Kasetsart J. (Nat. Sci.) 47 : 953 - 966 (2013)

A Land Cover Mapping Algorithm Based on a Level Set Method

Teerasit Kasetkasem[1,*], Settaporn Sriwilai[1], Thitiporn Chanwimaluang[2] and Tsuyoshi Isshiki[3]

ABSTRACT

A novel supervised classification algorithm is presented for remotely sensed images using the level set method under a statistical framework. The level set method was employed to capture the connectivity properties of land cover classes. This work demonstrated that land cover mapping under the maximum *a posteriori* criteria can be converted into an energy minimization problem of level set functions. Since the level set functions are real-valued, the optimum solution can be easily obtained from a gradient search technique. The experimental results showed significant improvements in term of the classification performance of the approach on both synthetic and satellite images when compared to the maximum likelihood classifier.

Keywords: image classification, land cover mapping, image segmentation, level set method

INTRODUCTION

Remote sensing images are widely used in a wide range of fields such as natural resource monitoring, urban planning, hazard assessment and especially land cover mapping. Image classification or land cover mapping is one of the most important applications of remote sensed images. The task of image classification is to categorize a pixel or group of pixels in a remote sensing image into one of several homogeneous land cover classes. Although this task is usually simple for trained personnel, it is difficult to program and hence, there is always a need for more sophisticated image classification algorithms. Gao and Mas (2008) considered two different kinds of classification methods—namely pixel-based and region-based classifications. In pixel-based methods (Wang *et al.,* 2006), a feature vector corresponding to the detailed spectrum of reflected light is assigned to each pixel in an image. Then, by using these feature vectors, each pixel can be labeled into one of the designated land cover classes by comparison with all signature vectors of the classes of interest. Basically, a pixel will be labeled as Class *A* if its feature vector is closest to the signature vector of Class *A*. In region-based methods (Tarabalka *et al*. 2009), firstly, the image is divided into many regions using an image segmentation algorithm. Then, each region is classified into a land cover class based on its averaged feature vector in the region. The region-based approach is suitable for land cover mapping on remote sensing images since the land cover classes are likely to appear in connected regions rather than as isolated pixels. However, since region-based approaches

1 Department of Electrical Engineering, Faculty of Engineering, Kasetsart University Bangkok 10900, Thailand.

2 Image Technology Laboratory, National Electronics and Computer Technology Center, Pathum Thani 12120, Thailand.

3 Department of Communications and Integrated Systems, Tokyo Institute of Technology, Ookayama, Meguro-ku, Tokyo 152-8550, Japan.

* Corresponding author, email: fengtsk@ku.ac.th

Received date : 30/05/13 Accepted date : 15/08/13

assign an entire region to one land cover class, the performance of this approach can be severely degraded in a scenario where the signal to noise ratio is low (Tarabalka *et al*., 2009). The approach that incorporates the spatial dependency of the land cover class among neighboring pixels into the pixel-based image classification should be more robust when dealing with severe noise than the region-based approaches since the effect of noise can be minimized when information from the neighboring pixels is incorporated (Kasetkasem and Varshney, 2003).

Consequently, the objective of this paper was to combine the pixel-based and region-based algorithms for land cover mapping of remotely sensed images. Instead of assigning a pixel to one of the listed land cover classes, the approach used determined the edge of each land cover class such that the entire region inside the edge belongs to only one land cover class. To find the edge between land cover classes, the land cover mapping problem was modified into an image segmentation problem where active contour models can be applied. The active contour model was first introduced by Kass *et. al.* (1987) as an image segmentation algorithm to segment objects in an image using dynamic curves. The current approach aimed to model the dynamic curves as a snake that attempts to rest on the edges among homogenous regions. The resultant position of the snake corresponds to the minimization of an energy function. In fact, energy minimization approaches have been applied successfully in various image processing problems such as Kasetkasem and Varshney (2002, 2003), Kasetkasem *et al.* (2005), Kasetkasem and Varshney (2011) and Hachama *et al.* (2012). In recent years, the active contour model has been popularly implemented using the level set method (Osher and Sethian, 1988) and is called the geometric active contour model. In this model, contours are represented as the zero level set of a higher dimensional function that may break or merge naturally during the evolution, and the topological changes are thus automatically handled. Therefore, the geometric model is suitable for the proposed approach algorithm.

MATERIAL AND METHODS

Problem statement

Let $X(\mathcal{S})$ denote the land cover map (LCM) where $\mathcal{S}$ is a set of pixels. We assume that there are L land cover classes in the area of interest and we let $\Lambda \in \{0, 1,\ldots, L-1\}$ be the class labels. Therefore, we can express the LCM as $X(\mathcal{S}) \in \Lambda^{\mathcal{S}}$. The label of LCM at pixel s = (u, v) is denoted by x_s which can also be called the configuration of $X(\mathcal{S})$ at the site s. The goal of the LCM is to label each pixel in the image into one of the known land cover classes. Figure 1 shows an example of the labeling of a two-class LCM. Here, the pixels outside and inside the rectangular box are labeled as one and two to indicate that they belong to Classes 1 and 2, respectively. As an alternative to labeling each pixel, one can also consider the land cover mapping process as a border extraction problem; that is, we want to find the borders between classes. For instance, if we extract the border (Figure 2) between Class 1 and Class 2 in Figure 1, we can identify that all pixels outside and inside the border belong to Classes 1

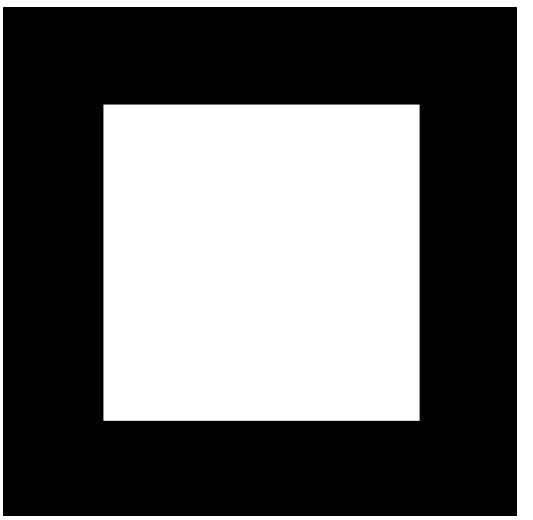

Figure 1 Example of a two-class land cover map.

and 2, respectively. There are many approaches to represent borders. For instance, a border may be modeled as piece-wise continuous lines (Kass *et al.*, 1987) or graphs of vertices and borders (Osher and Sethian, 1988). A more interesting idea is to represent contours as the zero level set of a higher dimensional function (such as two dimensional to three dimensional) called the signed distance function.

The signed distance function determines the distance of a given point s from the boundary Ω in a space. Here, the sign is used to indicate whether s is inside or outside Ω. In this paper, we denote $\phi_l(\mathcal{S}_R)$ for $l \in \Lambda$ as a signed distance function for Class l defined in a domain $\mathcal{S}_R \subset \Re^2$ where $\Re$ denotes the set of real numbers. The domain $\mathcal{S}_R$ is called the extended pixel domain, and can be viewed as an extension of $\mathcal{S}$ that includes non-integer coordinates.Since $\phi_l(\mathcal{S}_R)$ is the signed distance function, the value of $\phi_l(s)$ represents how far a pixel s is from the edge, as given by Equation 1:

$$\phi_l(s) = \begin{cases} d(s, \Omega_l) if\ x(s) = l \\ -d(s, \Omega_l) if\ x(s) \neq l \end{cases} \quad (1)$$

where Ω_l is the border of the land cover class l and $d(s, \Omega_l)$ is the shortest distance from s to the border Ω_l. For example, there are two signed distance functions, $\phi_1(s)$ and $\phi_2(s)$, indicating whether a pixel s is inside the border of Classes 1 or 2, respectively. Figures 3a and 3b display the signed distance functions with respect to Class 1 and Class 2, respectively, of the LCM given in Figure 1. We observe that, for pixels inside the border given in Figure 2, $\phi_1(s)$ is negative whereas $\phi_2(s)$ is positive. The signs of $\phi_1(s)$ and $\phi_2(s)$ are reversed when a pixel is outside the border given in Figure 2. In fact, we have $\phi_1(s) = -\phi_2(s)$. Note here that both signed distance functions are zero at the border pixels in Figure 2.

From the definition of the signed distance function, we can represent the LCM as Equation 2:

$$X(\mathcal{S}) = \sum_{l=0}^{L-1} l H(\phi_l(\mathcal{S})) \quad (2)$$

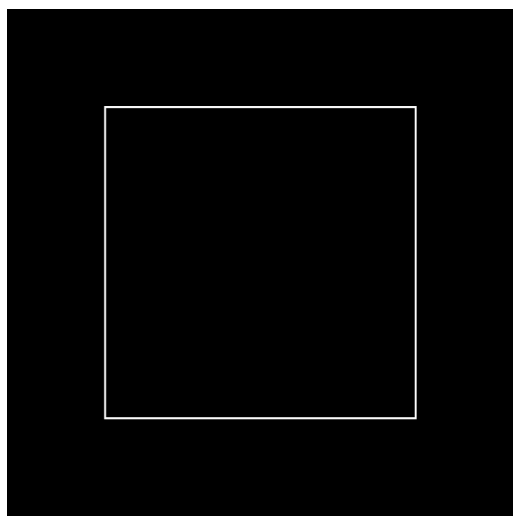

Figure 2 Border of the land cover map given in Figure 1.

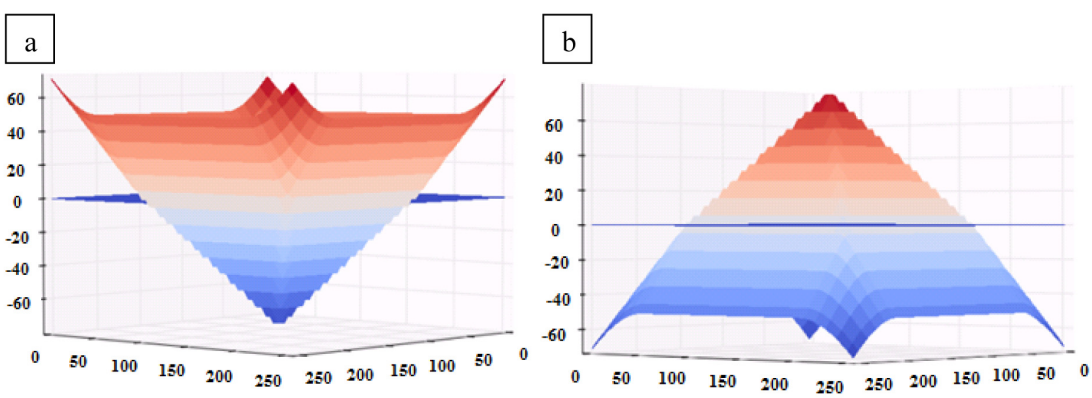

Figure 3 Signed distance functions of (a) Class 1 and (b) Class 2 for the land cover map in Figure 1.

where H(z) is the Heaviside function defined as shown in Equation 3:

$$H(z)=\begin{cases}0, & x<0\\ 1, & x\geq 0\end{cases} \quad (3)$$

Since the LCM is a function of the level set function, the probability density function of the LCM is the function of all signed distance functions (Equation 4):

$$\Pr(X)=\Pr(\phi_0,\ldots,\phi_{L-1}) \quad (4)$$

Here and throughout the rest of the paper, we omit ($\mathcal{S}$) for the sake of abbreviation. Hence, the marginal probability density function of the LCM can be written as Equation 5:

$$\Pr(X)=\Pr(\boldsymbol{\phi})=\frac{\exp\left[-E_X(\boldsymbol{\phi})\right]}{Z} \quad (5)$$

where $\boldsymbol{\phi}=\{\phi_0,\ldots,\phi_{L-1}\}$ is the collection of all signed distance functions, Z is the normalizing constant and $E_x(\boldsymbol{\phi})$ is the LCM energy function depending on the value of $\phi_0,\ldots,\phi_{L-1}$. This energy function should be defined such that land cover classes are more likely to appear as a connected region rather than as isolated pixels and all pixels in the LCM must belong to one and only one land cover class. Here, we apply the idea of the level set method proposed in Chan and Vese (2001) to model $E_x(\boldsymbol{\phi})$, and we have Equation 6:

$$E_x(\boldsymbol{\phi})=E_p(\boldsymbol{\phi})+E_l(\boldsymbol{\phi})+E_a(\boldsymbol{\phi}). \quad (6)$$

The first energy term, E_p, ensures that ϕ_l is a valid signed distance function and we define the energy term as Equation 7:

$$E_p(\boldsymbol{\phi})=\sigma\sum_{l=0}^{L-1}\sum_{s\in\mathcal{S}}\frac{1}{2}\left(\left|\nabla\phi_l(s)\right|-1\right)^2 \quad (7)$$

where ∇ is the gradient operation and α is a non-negative constant. This term imposes the condition that all signed distance functions in the Euclidean space must have the magnitude of the gradient equal to one, that is, $|\nabla\phi_l(s)|=1$ (Li *et al*., 2005).

The second and third energy terms, E_l and E_a , represent the length (Li *et al*., 2005) and the area (Li *et al*., 2005) of the zero level curve $\phi_l(s)$, and are defined by Equation 8:

$$E_l(\boldsymbol{\phi})=\lambda\sum_{l=0}^{L-1}\sum_{s\in\mathcal{S}}c\left(\phi_l(s)\right)\left|\nabla\phi_l(s)\right|, \quad (8)$$

and Equation 9:

$$E_a(\boldsymbol{\phi})=\sum_{l=0}^{L-1}\nu_l\sum_{s\in\mathcal{S}}H\left(\phi_l(s)\right) \quad (9)$$

respectively. Here, c(.) is one if $\phi_l(s)$ changes sign within a pixel s, λ is a non-negative constant and ν_1 can be positive or negative. We observe that the terms $c(\phi_1(s))|\nabla\phi_1(s)|$ in Equation 8, and $H(\phi_1(s))$ in Equation 9 have non-zero values only on and inside the border of Class l, respectively. As a result, a land cover class associated with a large value of ν_1 is penalized more, and is less likely to occur in the LCM.

Next, we denote $Y(\mathcal{S})$ as the observed multispectral image whose observation at a pixel s can be represented in the vector form as $y_s\in\Re^B$ where B is the number of spectral bands. Here, we assume further that observed data at different pixels are statistically independent for a given LCM, as shown by Equation 10:

$$\Pr(Y|X)=\prod_{s\in\mathcal{S}}\Pr(\mathbf{y}_s|x_s). \quad (10)$$

By using the representation given in Equation 2, the conditional probability can be written as a function of $\phi_0,\ldots,\phi_{L-1}$ as

$$\Pr(Y|X)=\Pr(Y|\boldsymbol{\phi})=\prod_{s\in\mathcal{S}}\sum_{l=0}^{L-1}\Pr(\mathbf{y}_s|x_s=l)H(\phi_l) \quad (11)$$

In this paper, the observed vector for a given land cover class is assumed to be multivariate Gaussian distributed (Equation 12):

$$\Pr(\mathbf{y}_s|x_s)=\frac{\exp\left[-\frac{1}{2}\left(\mathbf{y}_s-\boldsymbol{\mu}_{x_s}\right)^T\Sigma_{x_s}^{-1}\left(\mathbf{y}_s-\boldsymbol{\mu}_{x_s}\right)\right]}{(2\pi)^{\frac{B}{2}}\left|\Sigma_{x_s}\right|^{\frac{1}{2}}} \quad (12)$$

where $\boldsymbol{\mu}_{x_s}$ and E_{x_s} are the mean vector and covariance matrix of the land cover class x_s. By substituting Equation 12 into Equation 11, the conditional probability becomes Equation 13:

$$\Pr(Y|\boldsymbol{\phi})=\frac{\exp\left[-E(Y|\boldsymbol{\phi})\right]}{Z_Y} \quad (13)$$

where Equation 14 defines the relevant term:

$$E(Y|\boldsymbol{\phi})=\frac{1}{2}\sum_{l=0}^{L-1}\sum_{s\in\mathcal{S}}H\left(\phi_l(s)\right)\left[\left(\mathbf{y}_s-\boldsymbol{\mu}_l\right)^T\Sigma_l^{-1}\left(\mathbf{y}_s-\boldsymbol{\mu}_l\right)\right.$$

$$+\ln\left|\Sigma_l\right|\Big], \quad (14)$$

and Z_Y is a normalizing constant. Note again that the term $H(\phi_l(s))$ is one if $\phi_l(s) > 0$ and zero otherwise.

By using the chain rule, the *a posteriori* probability of the LCM given the observed multispectral images can be written as Equation 15:

$$\Pr(X|Y) = \Pr(\boldsymbol{\phi}|Y) = \frac{\Pr(Y|\boldsymbol{\phi})\Pr(\boldsymbol{\phi})}{\Pr(Y)}. \quad (15)$$

Since Pr(Y) is independent of the choice of $\boldsymbol{\phi}$, it can be treated as a constant. Hence, we have Equation 16:

$$\Pr(\boldsymbol{\phi}|Y) = C\prod_{s\in\mathcal{S}} \Pr(Y|\boldsymbol{\phi})\Pr(\boldsymbol{\phi}). \quad (16)$$

By substituting Equation 13 into Equation 16, we obtain Equation 17:

$$\Pr(\boldsymbol{\phi}|Y) = \frac{1}{Z'}\exp\left[-E(\boldsymbol{\phi}|Y)\right], \quad (17)$$

where Z' is a normalizing constant and independent of the choice of X, and Equation 18:

$$E(\boldsymbol{\phi}|Y) = E_X(\boldsymbol{\phi}) + E(Y|\boldsymbol{\phi}). \quad (18)$$

By substituting Equation 6 – Equation 9 and Equation 14 into Equation 18, we obtain Equation 19:

$$\begin{aligned} E(\boldsymbol{\phi}|Y) = &\sum_{l=0}^{L-1}\sum_{s\in\mathcal{S}} \frac{\alpha}{2}\left(\left|\nabla\phi_l(s)\right|-1\right)^2 + \\ &\sum_{l=0}^{L-1}\sum_{s\in\mathcal{S}} \lambda c(\phi_l(s))\left|\nabla\phi_l(s)\right| + \\ &\sum_{l=0}^{L-1}\sum_{s\in\mathcal{S}} \nu_l H(\phi_l(s)) + \\ &\frac{1}{2}\sum_{l=0}^{L-1}\sum_{s\in\mathcal{S}} H(\phi_l)\Big[(\mathbf{y}_s-\boldsymbol{\mu}_l)^T \\ &\Sigma_l^{-1}(\mathbf{y}_s-\boldsymbol{\mu}_l) + \ln\left|\Sigma_l\right|\Big] \end{aligned} \quad (19)$$

Next, we approximate the summation over all pixels in $\mathcal{S}$ by the integration over $\mathcal{S}_R$ and the above equation can be written as Equation 20:

$$\begin{aligned} E(\boldsymbol{\phi}|Y) \approx \sum_{l=0}^{L-1}\int_{s\in\mathcal{S}_R} \Big\{ &\frac{\alpha}{2}\left(\left|\nabla\phi_l\right|-1\right)^2 + \lambda\delta(\phi_l)\left|\nabla\phi_l\right| + \nu_l H(\phi_l) \\ &+ \frac{1}{2}H(\phi_l)\Big[(\mathbf{y}_s-\boldsymbol{\mu}_l)^T\Sigma_l^{-1}(\mathbf{y}_s-\boldsymbol{\mu}_l) + \ln\left|\Sigma_l\right|\Big]\Big\} ds \end{aligned} \quad (20)$$

Note here that we replace the function c(.) by the impulse function δ(.) since $\int_{s\in\mathcal{S}_R}\delta(\phi_l)ds$ is the length of the border of Class l. We also omit the term (s) for the sake of abbreviation.

Optimum land cover mapping problem

The classifier based on the maximum *a posteriori* (MAP) criterion selects the most likely LCM among all possible LCMs given the observed image. The resulting probability of error is the minimum among all other classifiers. The MAP criterion is expressed as Equation 21 (Van Trees, 1968 and Varshney 1997):

$$X^{opt} = \arg\max_X\left[\Pr(X|Y)\right] \quad (21)$$

In general, Pr(X|Y) is a non-convex function and, therefore, a conventional optimization algorithm may not be applicable to solve Equation 21. Furthermore, the number of possible LCMs is extremely large. For instance, there are more than 1.267×10^{30} possible LCM images assuming that an LCM is a binary image (having only two classes) of size 10 × 10 pixels. For multiclass problems such as land cover classification, this number increases greatly. As a result, in this paper, we propose to find the optimum solution with respect to ϕ_l instead. By using Equations 15 and 17, the optimization problem becomes Equation 22:

$$\boldsymbol{\phi}^{opt} = \arg\min_{(\boldsymbol{\phi})}\left[E(\boldsymbol{\phi}|Y)\right] \quad (22)$$

Optimization algorithm

Here, we assume that an analyst selects a sufficient number of training pixels from the observed image. These training pixels are used to estimate the unknown parameters (for example, mean vectors and covariance matrices) used in the characterization of each land cover classes. From our image model, and since $\phi_0, \ldots, \phi_{L-1}$ are real-value functions, the optimum solution of Equation 22 can be obtained by letting the derivative of $E(\boldsymbol{\phi}|Y)$ with respect to ϕ_l for be equal to zero (Equation 23):

$$\frac{\partial}{\partial\phi_l}E(\boldsymbol{\phi}|Y) = 0; \quad l = 0,1,\ldots,L-1. \quad (23)$$

By the calculus of variations (Li *et al*., 2005), the first variation of the above energy function can be written as Equation 24:

$$\frac{\partial \mathrm{E}\left(\phi_{\mathrm{o}},\ldots,\phi_{\mathrm{L}-1}|\mathrm{Y}\right)}{\partial \phi_{\mathrm{l}}}$$

$$\approx -\alpha\left[\phi_{\mathrm{l}}-\mathrm{div}\left(\frac{\nabla\phi_{\mathrm{l}}}{|\nabla\phi_{\mathrm{l}}|}\right)\right]-\lambda\delta\left(\phi_{\mathrm{l}}\right)\mathrm{div}\left(\frac{\nabla\phi_{\mathrm{l}}}{|\nabla\phi_{\mathrm{l}}|}\right)+\nu_{\mathrm{l}}\delta\left(\phi_{\mathrm{l}}\right)$$

$$+\frac{1}{2}\delta\left(\phi_{\mathrm{l}}\right)\left[\left(\mathrm{y_s}-\mu_{\mathrm{l}}\right)^{\mathrm{T}}\Sigma_{\mathrm{l}}^{-1}\left(\mathrm{y_s}-\mu_{\mathrm{l}}\right)+\ln|\Sigma_{\mathrm{l}}|\right] \quad (24)$$

where Δ is the Laplacian operator (Evans, 1998) and div is the Divergence operator (Evans, 1998). Therefore, the function ϕ that minimizes this function satisfies the Euler Lagrange equations $\frac{\partial \mathrm{E}\left(\phi_{\mathrm{o}},\ldots,\phi_{\mathrm{L}-1}|\mathrm{Y}\right)}{\partial \phi}=0$. The steepest descent process for minimization of the function $\mathrm{E}\left(\phi_{\mathrm{o}},\ldots,\phi_{\mathrm{L}-1}|\mathrm{Y}\right)$ can be employed and we have Equation 25:

$$\phi_{\mathrm{l}}^{\mathrm{k}+1}=\phi_{\mathrm{l}}^{\mathrm{k}}-\tau\frac{\partial \mathrm{E}\left(\phi_{\mathrm{o}}^{\mathrm{k}},\ldots,\phi_{\mathrm{L}-1}^{\mathrm{k}}|\mathrm{Y}\right)}{\partial \phi_{\mathrm{l}}} \quad (25)$$

where the superscript k = 0,1,2, … denotes the iteration number, $\tau > 0$ is the step size and ϕ_{l}^{0} is the initial signed distance function of Class l. In this work, the initial signed distance functions are derived from the initial LCM denoted by $\mathrm{X_{init}}$. Here, the signed distance function at a pixel s of Class l is set to a positive value ρ if a pixel s in the initial LCM belongs to Class l, and is set to $-\rho$, otherwise (Equation 26):

$$\phi_{\mathrm{l}}^{0}\left(\mathrm{s}\right)=\begin{cases}\rho, & \mathrm{x_{init}}\left(\mathrm{s}\right)=\mathrm{l}\\ -\rho, & \mathrm{x_{init}}\left(\mathrm{s}\right)\neq\mathrm{l}\end{cases} \quad (26)$$

where $\mathrm{X_{init}(s)}$ is the label of a pixel s in the initial LCM. Note here that, in this paper, ρ is equal to 2.

Since the derivative given in Equation 24 involves the impulse function, the derivative cannot be computed numerically. As a result, we follow the work of Samson *et al.* (2000) by approximating the Heaviside and impulse functions as Equation 27:

$$\mathrm{H}_{\epsilon}\left(\phi_{\mathrm{i}}\right)=\begin{cases}\frac{1}{2}\left(1+\frac{\phi}{\epsilon}+\frac{1}{\pi}\sin\left(\frac{\pi\phi}{\epsilon}\right)\right), & |\phi|\leq\epsilon\\ 1, & \phi>\epsilon\\ 0, & \phi<-\epsilon,\end{cases} \quad (27)$$

and Equation 28:

$$\delta_{\epsilon}\left(\phi_{\mathrm{i}}\right)=\frac{\mathrm{dH}_{\epsilon}\left(\phi_{\mathrm{i}}\right)}{\mathrm{d}\phi_{\mathrm{i}}}=\begin{cases}\frac{1}{2\phi}\left(1+\cos\left(\frac{\pi\phi}{\epsilon}\right)\right), & |\phi|\leq\epsilon\\ 0, & |\phi|>\epsilon,\end{cases} \quad (28)$$

respectively. Here ϵ is a small positive value and, in this paper, we use the value of ϵ equal to 1.0.

By applying the approximation given in Equation 28 into Equation 24, the first variation can be approximated as Equation 29:

$$\frac{\partial \mathrm{E}\left(\phi_{\mathrm{o}},\ldots,\phi_{\mathrm{L}-1}|\mathrm{Y}\right)}{\partial \phi_{\mathrm{l}}}\approx\Delta\mathrm{E}_{\mathrm{l}} \quad (29)$$

where (Equation 30):

$$\Delta\mathrm{E}_{\mathrm{l}}=-\alpha\left[\phi_{\mathrm{l}}-\mathrm{div}\left(\frac{\nabla\phi_{\mathrm{l}}}{|\nabla\phi_{\mathrm{l}}|}\right)\right]-\lambda\delta_{\epsilon}\left(\phi_{\mathrm{l}}\right)\mathrm{div}\left(\frac{\nabla\phi_{\mathrm{l}}}{|\nabla\phi_{\mathrm{l}}|}\right)$$

$$+\nu_{\mathrm{l}}\delta_{\epsilon}\left(\phi_{\mathrm{l}}\right)+\delta_{\epsilon}\left(\phi_{\mathrm{l}}\right)\left[\left(\mathrm{y_s}-\mu_{\mathrm{l}}\right)^{\mathrm{T}}\Sigma_{\mathrm{l}}^{-1}\left(\mathrm{y_s}-\mu_{\mathrm{l}}\right)+\ln|\Sigma_{\mathrm{l}}|\right] \quad (30)$$

Hence, from Equation 30, a new set of signed distance functions can be obtained from Equation 31:

$$\Phi^{\mathrm{k}+1}=\Phi^{\mathrm{k}}-\tau\Delta\Phi^{\mathrm{k}} \quad (31)$$

where $\Phi^{\mathrm{k}}=\begin{bmatrix}\phi_0^{\mathrm{k}} & \cdots & \phi_{\mathrm{L}-1}^{\mathrm{k}}\end{bmatrix}^{\mathrm{T}}$ is a vector of the signed distance functions at a pixel and $\Delta\Phi^{\mathrm{k}}=\begin{bmatrix}\Delta\mathrm{E}_0 & \cdots & \Delta\mathrm{E}_{\mathrm{L}-1}\end{bmatrix}^{\mathrm{T}}$ is the updating vector for the $\mathrm{k^{th}}$ iteration. Here, $(.)^{\mathrm{T}}$ denotes the matrix transpose operation.

For a given pixel, the new set of signed distance functions given in Equation 31 can lead to three scenarios: 1) only one signed distance function is greater than zero; 2) two or more signed distance functions are greater than zero; and 3) no signed distance function is greater than zero. In the first scenario, one and only one land cover class will be presented on a given pixel whereas the second and third scenarios correspond to cases where more than one land cover class are present and all land cover classes are absent on a pixel, respectively. Clearly, the second and third scenarios produce an invalid LCM. As a result, we propose to limit the update direction of Equation 31 to be in the region such that $\sum_{\mathrm{l}=0}^{\mathrm{L}-1}\mathrm{H}\left(\phi_{\mathrm{l}}\right)=1$ to ensure that one and only one land cover class is present on a given pixel. To do that, the update direction must be perpendicular to the gradient of

$\sum_{l=0}^{L-1} H_\epsilon(\phi_l) = 1$. Hence, the valid update direction is given by Equation 32:

$$\Delta\Phi^{*k} = \Delta\Phi^k - \langle \Delta\Phi^k, n \rangle n \quad (32)$$

where $\langle . , . \rangle$ is the inner product operation, and from Equation 33:

$$\Delta n = \frac{\left[\delta_\epsilon(\phi_0) \quad \cdots \quad \delta_\epsilon(\phi_{L-1})\right]^T}{\left[\delta_\epsilon(\phi_0) \quad \cdots \quad \delta_\epsilon(\phi_{L-1})\right]^T} \quad (33)$$

is the normalized gradient vector of $\sum_{l=0}^{L-1} H_\epsilon(\phi_l) = 1$. Again, we replace $H(\phi_1)$ with $H_\epsilon(\phi_1)$ due to the same implementation reason given early in this section. Figure 4 summarizes the proposed algorithm given in this section.

RESULTS AND DISCUSSION

The performance of the proposed algorithm was examined with simulated and actual satellite data sets. These experiments compared the performance of the algorithm with the maximum likelihood classifier (MLC) since the MLC is well-known and widely used in remote sensing image classification (Richards and Xiuping, 1999).

Simulated dataset

The simulated experiment used the 256 × 256 pixel gray scale image with two classes with mean values of 0 and 100 for Classes 0 and 1, respectively. Figure 5 displays the ground truth image used in this example. Note here that Class 1 appears as a ring in Figure 5. Next, the independent additive Gaussian noises with zero mean and standard deviation of σ were added to all pixels in the noiseless image to produce the observed noisy image. The values of σ were varied from 10 to 1,000 to simulate different level of randomness. For σ = 10, the signal to noise ratio (SNR) of the observed noisy image was equal to 20 dB while, for σ = 1,000, the SNR was equal to dB. Figures 6a—6c show the noisy images for the SNRs equal to 20, -2.22, -20dB, respectively.

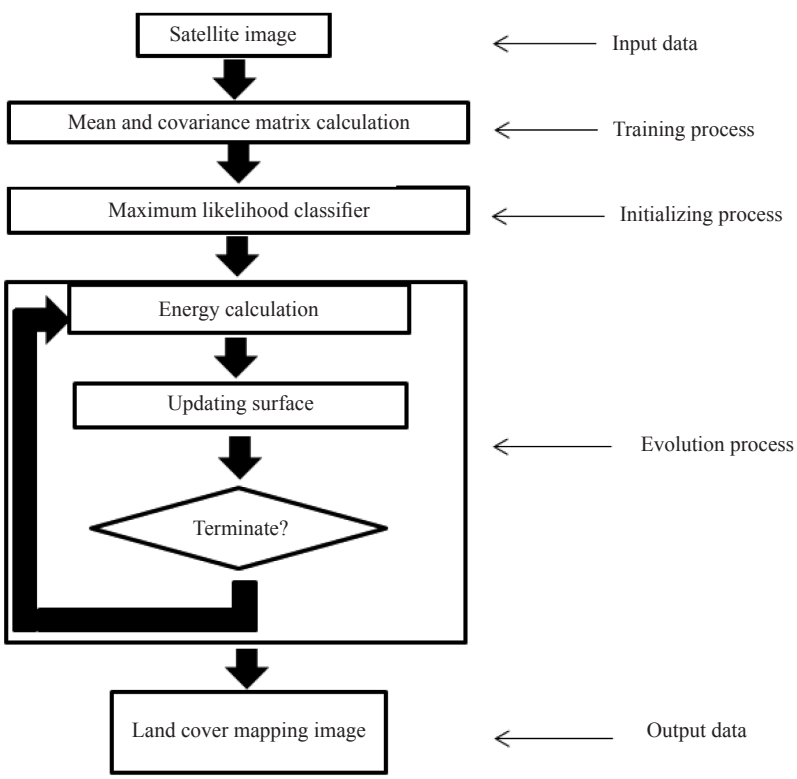

Figure 4 Flow chart for proposed algorithm.

Next, the noisy images were initially classified using the maximum likelihood classifier (Wang *et al.*, 2006) based on the given mean values and noise standard deviation. The initial classified images are given in Figures 7a–7c for various noise levels. As the noise standard deviation increased, the number of isolated pixels increased. In particular, for the noise standard deviation equal to 1,000, the initial LCM became very noisy and the structure of the ring disappeared. The percentages of correctly classified pixels of the initial LCMs for σ equal to 10, 129.15 and 1,000 were 100, 65.12 and 52.32%, respectively.

Figure 5 Synthetic image with two classes.

These initial LCMs were submitted to the proposed algorithm and the resulting LCMs obtained from the algorithms after 1,000 iterations for the parameter setup of $\alpha = 0.05$, $\lambda = 30.0$, $\nu_0 = \nu_1 = -15.0$, and $\tau = 0.003$ are shown in Figures 8a–8c, which show that the algorithm can successfully extract the ring structure back for $\sigma = 10$ and 129.15. However, the algorithm could only partially extract the ring structure back from

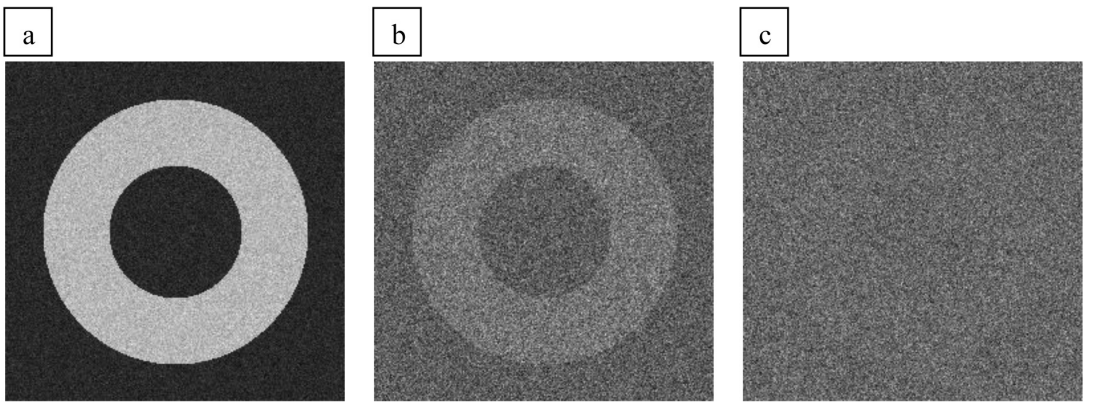

Figure 6 Noisy images with signal to noise ratio of: (a) 20dB, (b) -2.22dB and (c) -20dB.

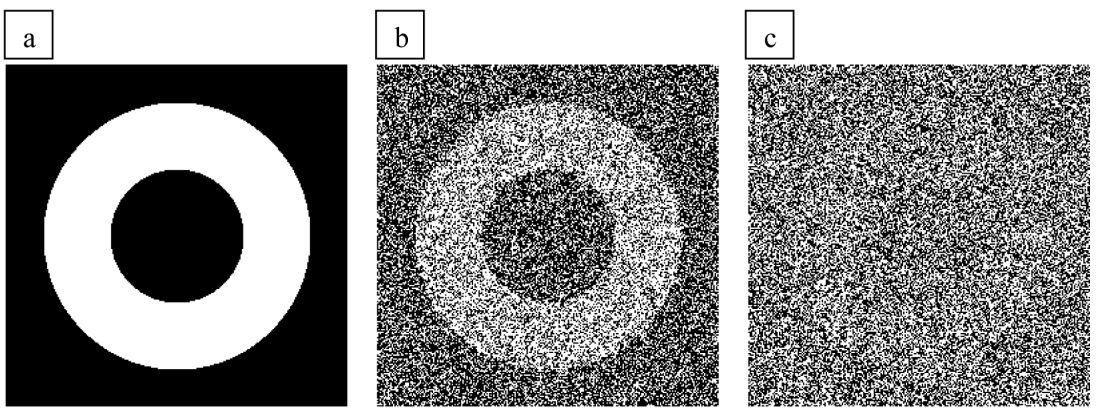

Figure 7 Classified images using the maximum likelihood functions with signal to noise ratio of: (a) 20dB, (b) -2.22dB and (c) -20dB.

the noisy observed image for the case where σ = 1,000. The percentages of correctly classified pixels obtained from the proposed algorithm for σ equal to 10, 129.15 and 1,000 were 100, 86.96 and 65.49%, respectively.

Next, the above experiment was repeated 50 times and the averaged percentages of correctly classified pixels obtained from the proposed algorithm and the maximum likelihood classified are summarized in Table 1. From the *t*-statistics and the critical value for 5% type I error given in Table 1, the resulting LCMs obtained from the proposed algorithm were significantly better than those obtained from the MLC for σ = 16.68 – 215.44. In fact, only at very high SNR (σ = 10) did both the proposed algorithm and the MLC perform similarly because both algorithms made very few classification errors.

Satellite data set

A multispectral image of a part of the Kasetsart University campus, Bangkok, Thailand from the QuickBird satellite (Figure 9) and ground data obtained by visual reference (Figure 10) were used for this experiment. Eight land cover classes were identified—grass, water, road,

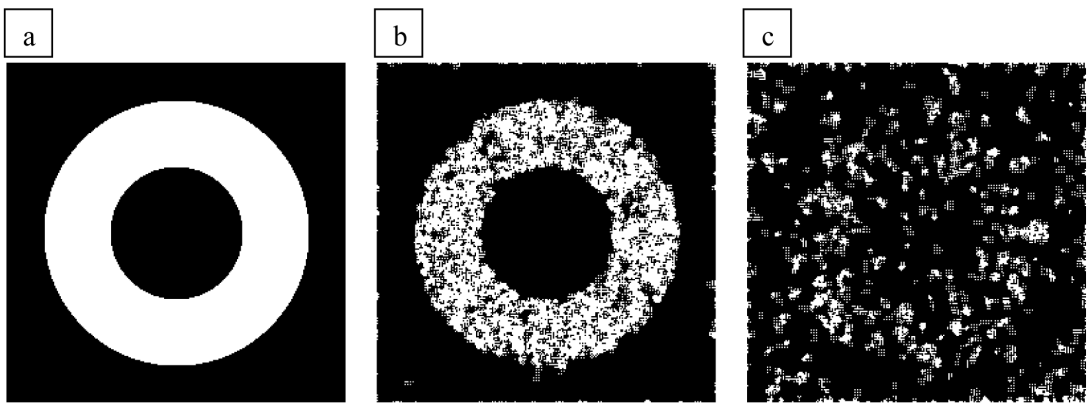

Figure 8 Classified images using the proposed method with signal to noise ratio of: (a) 20dB, (b) -2.22dB, (c) -20dB.

Table 1 Percentages of correctly classified pixels for various noise levels.

Noise standard deviation	SNR	MLC		Proposed Algorithm		*t*-statistic	Critical Value for 5% Type I Error
		Mean	SD	Mean	SD		
10	20.0	100.0	0.0002	100.0	0.0	0.0	2.010
16.68	15.56	99.86	0.017	100.0	0.0026	7.91*	2.010
27.83	11.11	96.39	0.0644	99.92	0.0128	380.12*	2.010
46.42	6.67	85.91	0.129	99.14	0.0444	685.832*	2.000
77.43	2.22	74.08	0.1313	95.26	0.1611	720.623*	1.986
129.15	-2.22	65.05	0.192	87.18	0.3668	377.868*	1.993
215.44	-6.67	59.16	0.1799	78.36	0.4958	257.473*	2.000
359.38	-11.11	55.50	0.1969	71.67	0.7147	154.23*	2.003
599.48	-15.55	53.3003	0.1927	67.1867	0.5807	-160.48*	2.001
1000	-20.0	52.0265	0.171	64.3973	0.6008	-140.04*	2.003

SNR = Signal to noise ratio; MLC = Maximum likelihood classifier.

* = Significant difference at $P < 0.05$ level of testing.

shadow, building1, building2, building3 and tree. Building1, building2 and building3 corresponded to different roof colors in the satellite image. In the first stage, mean vectors and covariance matrices were estimated for all classes by manually selecting 1,242, 1,481, 1,144, 2,501, 4,012, 2,667, 3,023 and 22,870 pixels for building1, building2, building3, grass, water, road, shadow and tree, respectively. The mean vectors for the eight classes are given in Table 2 (the covariance matrices are not shown for brevity). These mean vectors and the covariance matrices were used to obtain the initial LCM (Figure 11). A visual comparison between the initial LCM and the ground data (Figure 10) illustrates the poor performance of the MLC since there are many isolated pixels in the initial LCM. Next, the initial LCM, mean vectors and covariance matrices were input to the proposed algorithm and the resulting LCM after 2,200 iterations is displayed in Figure 12. In this experiment, the level set parameters were: $\alpha = 1.0$, $\lambda = 25.0$, $\nu_{grass} = \nu_{water} = \nu_{road} = \nu_{shadow} = \nu_{building1} = \nu_{building2} = \nu_{building3} = \nu_{tree} = 35.0$, and $\tau = 0.0005$.

By visual inspection of Figures 11 and 12, the resulting LCM obtained from the proposed algorithm is more connected with a substantial performance improvement over the initial LCM. Furthermore, the LCM in Figure 12 matched well with the reference data in terms of the smoothness of the classes. There were many mislabeled

Figure 9 Multispectral (Quickbird) image of a part of Kasetsart University, Bangkok, Thailand.

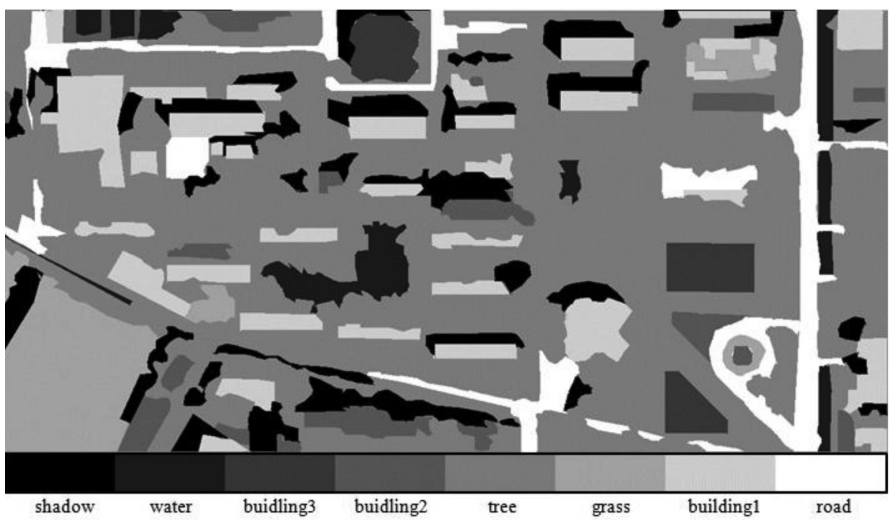

Figure 10 Ground data for sample area at Kasetsart University campus, Bangkok, Thailand.

pixels between the classes of tree and grass in the initial LCM. However, these mislabeled pixels disappeared in the resulting LCM. For the quantitative performance evaluation, the confusion matrices for the initial LCMs and the resulting LCMs are shown in Tables 3 and 4. The majority of pixels belonged to the tree class. From Tables 3 and 4, the percentages of correctly classified pixels for the initial and resulting LCMs were 54.52 and 71.03%, respectively. The performance difference of more than 15% demonstrates the superior performance of the proposed algorithm.

Table 2 Mean vectors for all classes for sample area at Kasetsart University campus, Bangkok, Thailand.

	Red	Blue	Green	Near Infrared
Building1	235.8	295.6	148.3	163.4
Building2	333.2	523.6	385.4	477.7
Building3	286.3	408.7	328.6	408.4
Grass	241.1	341.2	209.9	502.5
Water	260.7	357.0	228.2	304.2
Road	272.9	380.4	249.0	322.1
Shadow	230.4	288.7	155.3	210.6
Tree	232.7	306.7	172.0	387.5

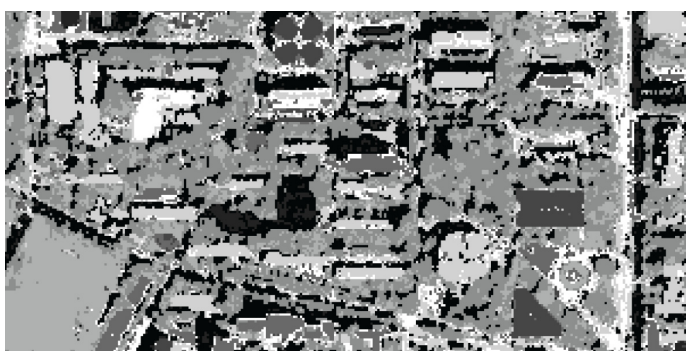

Figure 11 Initial land cover map for sample area at Kasetsart University campus, Bangkok, Thailand.

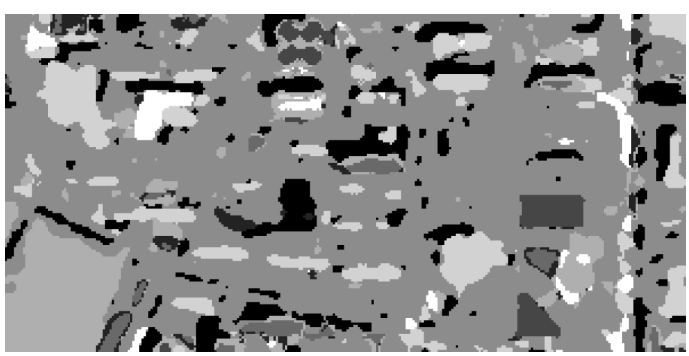

Figure 12 Resulting land cover map for sample area at Kasetsart University campus, Bangkok, Thailand from proposed method after 2200 iterations.

Next, the producer (Table 5) and user (Table 6) accuracies were compared for each land cover class between the initial (MLC) and resulting LCMs. The producer accuracies for the classes of tree and grass increased while the accuracies of the other land cover classes decreased. In particular, the producer accuracy for tree increased more than 75% mainly because in the initial LCM (Figure11), a large number of pixels belonging to the tree class were mislabeled as grass. After applying the initial LCM to the proposed algorithm, these small mislabeled patches were removed and replaced by the surrounding tree class. Since the MAP criteria were employed in this paper, the goal of the proposed algorithm was to minimize the overall probability of misclassification for all land cover classes rather than the probability of misclassification for an individual land cover class. As a result, the overall misclassification probably depended substantially on the mislabeled pixels in the class of tree because the majority of the area of interest was covered by trees. For

Table 3 Confusion matrix for the initial land cover map for sample area at Kasetsart University campus, Bangkok, Thailand.

	Classified image								Number of ground data pixels
	Building1	Building2	Building3	Grass	Water	Road	Shadow	Tree	
Ground Data									
Building1	465	10	5	13	24	21	862	148	1548
Building2	4	1233	59	62	163	263	45	57	1886
Building3	3	75	1034	21	49	60	5	16	1263
Grass	2	71	38	2319	48	29	33	183	2723
Water	46	95	88	89	3205	585	461	297	4866
Road	21	176	82	143	1104	1215	368	295	3404
Shadow	204	107	22	75	364	177	2536	540	4025
Tree	222	520	245	3936	2313	984	4538	12527	25285
Number classified	967	2287	1573	6658	7270	3334	8848	14063	45000

Table 4 Confusion matrix for the resulting land cover map for sample area at Kasetsart University campus, Bangkok, Thailand.

	Classified image								Number of ground data pixels
	Building1	Building2	Building3	Grass	Water	Road	Shadow	Tree	
Ground Data									
Building1	238	2	0	46	2	0	762	498	1548
Building2	286	771	0	348	68	11	24	378	1886
Building3	13	0	886	129	6	1	20	208	1263
Grass	48	9	0	2418	24	9	27	188	2723
Water	39	0	22	151	2963	262	206	1223	4866
Road	71	8	0	291	473	687	73	1801	3404
Shadow	13	24	0	236	241	9	2010	1492	4025
Tree	121	27	37	811	870	72	1358	21989	25285
Number classified	829	841	945	4430	4647	1051	4480	27777	45000

the user accuracy, most land cover classes had higher accuracies when the resulting LCM was compared with the initial one. However, the classes of building1 and tree had low accuracies due to the increase in the mislabeled pixels in the resulting LCM. The main reason for the decrease in the user accuracy for the tree class was due to the small areas of roads, water and shadows that surrounded the trees and were classified in the tree class. Since the proposed algorithm promotes a more connected land cover map, the small patches of water, shadow and road were overwhelmed by the large patch of the tree class.

CONCLUSION

A novel supervised classification algorithm for remotely sensed images was presented using the level set method under a statistical framework. The land cover mapping problem was able to be converted to the energy minimization of the signed distance functions where the gradient search technique could be applied. As a result, the proposed method could be easily implemented. The performance of the proposed algorithm using synthetic and satellite images was demonstrated. The experimental results showed that the proposed algorithm could substantially outperform the maximum likelihood classifier for a simulated and real dataset.

ACKNOWLEDGMENT

This research was supported in part by the Kasetsart Research and Development Institute (KURDI) under Grant Number 127.55. This research work was also supported in part by the Thailand Advanced Institute of Science and

Table 5 Comparison of percentage producer accuracy from the initial (MLC) and the resulting land cover map (LCM) for sample area at Kasetsart University campus, Bangkok, Thailand.

Land cover class	MLC (%)	Resulting LCM (%)
Building1	30.04	15.37
Building2	65.38	40.88
Building3	81.87	70.15
Grass	85.16	88.80
Water	65.87	60.89
Road	35.69	20.19
Shadow	63.01	49.94
Tree	49.54	86.96

Table 6 Comparison of percentage user accuracy from the initial (MLC) and the resulting land cover map (LCM) for sample area at Kasetsart University campus, Bangkok, Thailand.

Land cover class	MLC (%)	Resulting LCM (%)
Building1	48.09	28.71
Building2	53.91	91.68
Building3	65.73	93.76
Grass	34.83	54.58
Water	44.09	63.75
Road	36.44	65.37
Shadow	28.66	44.87
Tree	89.08	79.16

Technology (TAIST), the National Science and Technology Development Agency (NSTDA), Tokyo Tech Institute of Technology and Kasetsart University (KU).

LITERATURE CITED

Chan, T. and L. Vese. 2001. Active contours without edges. **IEEE Trans. Imag. Proc**., 10: 266–277.

Evans, L. 1998. **Partial Differential Equations.** American Mathematical Society. Providence, RI, USA. 749 pp.

Gao, Y. and J.F. Mas. 2008. A comparison of the performance of pixel based and object based classifications over images with various spatial resolutions. **Online Journal of Earth Sciences** 2: 27–35.

Hachama, M., A. Desolneux and F. Richard. 2012. A Bayesian technique for image classifying registration. **IEEE Trans. Image Process** 21(9): 4080–4091.

Kasetkasem, T. and P.K. Varshney. 2003. Statistical characterization of clutter scenes based on a Markov random field model. **IEEE Trans. on Aerospace and Electronic Systems** 39: 1035–1050.

_____. 2002. An image change detection algorithm based on Markov random field models. **IEEE Trans. on Geoscience and Remote Sensing** 40: 1815–1823.

_____. 2011. An optimum land cover mapping algorithm in the presence of shadows. **IEEE J. Sel. Topics Signal Process** 5(3): 592–605.

Kasetkasem, T., M.K. Arora and P.K. Varshney. 2005. Super-resolution land cover mapping using a Markov random field based approach**. Remote Sens. Environ.** 96(3–4): 302–314.

Kass, M., A.Witkin and D. Terzopoulos. 1987. Snakes: Active contour models. **Intl J. Computer Vision** l: 312–333.

Li, C., C. Xu, C. Gui and M.D. Fox. 2005. Level set evolution without re-initialization: A new variational formulation. **Proc. IEEE Conference on Computer Vision and Pattern Recognition (CVPR)** 1: 430–436.

Osher, S. and J.A. Sethian. 1988. Fronts propagating with curvature-dependent speed algorithms based on Hamilton-Jacobi formulations. **J. Comp. Phys.** 79: 12–49.

Richards, J.A. and J. Xiuping. 1999. **Remote Sensing Digital Image Analysis.** Springer. New York, NY, USA. 363pp.

Samson, C., L. Blanc-Féraud, G.Aubert and J. Zerubia. 2000. A level set model for image classification. **Int. J. Comput. Vision** 40: 187–197.

Tarabalka, Y., J.A. Benediktsson and J. Chanussot. 2009. Spectral-spatial classification of hyperspectral imagery based on partitional clustering techniques. **IEEE Trans. Geosci. Remote Sens.** 47(8): 2973–2987.

Van Trees, H.L. 1968. **Detection, Estimation, and Modulation Theory.** Wiley. New York, NY, USA. 716 pp.

Varshney, P.K. 1997. **Distributed Detection and Data Fusion.** Springer. New York, NY, USA. 276pp.

Wang, Y., X. Shwen and J. Xie. 2006. A review of remote sensing image classification methods. **Remote Sensing Information** 2: 67–71.